

## THE EFFECTS OF IRRADIATION ON THE CLOUD EVOLUTION IN ACTIVE GALACTIC NUCLEI

DANIEL PROGA<sup>1</sup>, YAN-FEI JIANG<sup>2,3</sup>, SHANE W. DAVIS<sup>4</sup>, JAMES M. STONE<sup>2</sup> AND DANIEL SMITH<sup>1</sup>

*Draft version June 24, 2018*

### ABSTRACT

We report on the first phase of our study of cloud irradiation. We study irradiation by means of numerical, two-dimensional time-dependent radiation-hydrodynamic simulations of a cloud irradiated by a strong radiation. We adopt a very simple treatment of the opacity, neglect photoionization and gravity, and instead focus on assessing the role of the type and magnitude of the opacity on the cloud evolution. Our main result is that even relatively dense clouds that are radiatively heated (i.e., with significant absorption opacity) do not move as a whole instead they undergo a very rapid and major evolution in its shape, size and physical properties. In particular, the cloud and its remnants become optical thin within less than one sound crossing time and before they can travel over a significant distance (a distance of a few radii of the initial cloud). We also found that a cloud can be accelerated as a whole under quite extreme conditions, e.g., the opacity must be dominated by scattering. However, the acceleration due to the radiation force is relatively small and unless the cloud is optically thin the cloud quickly changes its size and shape. We discuss implications for the modelling and interpretation broad line regions of active galactic nuclei.

*Subject headings:* methods: numerical — hydrodynamics — instability — radiative transfer

### 1. INTRODUCTION

There are very many situations in astrophysics where one object or a group of objects is exposed to relatively strong radiation produced by a nearby external source. Examples of such situations include planets and moons irradiated by their host star, a star irradiated by its companion in a binary system, gas clouds irradiated by a nearby stellar cluster or by an active galactic nucleus (AGN), and finally an outer part of a flaring accretion disk irradiated by its inner part or by the accretor.

Radiative heating caused by irradiation can change the irradiated object in several ways, e.g., it could change its structure, shape, size and the overall appearance. It could also lead to a significant mass loss and even acceleration of the cloud away from the source of radiation (via the so-called rocket effect). To some degree, similar changes could be caused by the radiation force (i.e., without radiative heating).

Effects of irradiation are most profound (e.g., cause ablation and destruction) in cases where the radiation energy is relatively high and the mass of the irradiated object is small so that self-gravity is negligible. Such cases are relevant in a variety of astrophysical environments, e.g., in the interstellar medium (ISM) (e.g., Oort & Spitzer 1955; Bertoldi 1989; Bertoldi & McKee 1990; Bally 1995), in planetary nebulae (e.g., Mellema et al. 1998), near the central region of AGN (e.g., Mathews 1986, and references therein) and outside the AGN host galaxy, in the intergalactic medium (IGM) (e.g., Donahue & Shull 1987).

The key questions in this context include: How does

the radiation that is reflected, reprocessed, or transmitted by a cloud compare to the original external radiation? What aspects and to what degree can the observed structure and kinematics be accounted for by irradiation? What are the dominant processes responsible for dispersing the gas that was initially collected in the cloud? What are the dominant processes responsible for accelerating the cloud? Can a cloud be significantly accelerated before it is dispersed? How do the acceleration and dispersing rates compare with the cloud formation rate?

Answering these questions is hard from both observational and theoretical points of view because the evolution of real clouds is very complex and too slow to be measured directly by observations. In addition, only in a few cases are clouds well spatially resolved (i.e., those in the nearby ISM, e.g., (Bally 1995)). Proper modeling of the clouds is further complicated by the fact that many time-dependent and multi-dimensional processes and effects are involved, e.g., radiative transfer (RT), gas photoionization and heating, the subsequent development and propagation of ionization and thermal fronts (IF and TF, respectively) and of shocks and discontinuities. Generally, the cloud irradiation problem requires the simultaneous solving of radiation-hydrodynamic (R-HD) equations (examples of such studies include Lefloch & Lazareff 1994; Mellema et al. 1998; González et al. 2007; Raga et al. 2007). One important aspect of this problem is that irradiation is anisotropic and optically thick clouds will cast shadows. Therefore, the RT methods for solving the R-HD equation have to treat the shadows accurately (e.g., Davis et al. 2012; Jiang et al. 2012). Effects of magnetic fields and dust increase the level of complexity even more (e.g., Krause et al. 2012, and references therein).

#### 1.1. Simple Cases

However, under some special and idealized conditions, the solution to the problem of the evolution of a spher-

<sup>1</sup> Department of Astronomy, University of Las Vegas, Las Vegas, NV 89119, USA

<sup>2</sup> Department of Astrophysical Sciences, Princeton University, Princeton, NJ 08544, USA

<sup>3</sup> Harvard-Smithsonian Center for Astrophysics, 60 Garden St., Cambridge, MA 02138, USA

<sup>4</sup> Canadian Institute for Theoretical Astrophysics. Toronto, ON M5S3H4, Canada

ical cold cloud that is suddenly exposed to external radiation could be quite trivial. For example, in optically thin cases with pure absorption opacity, the radiation would propagate very fast (faster than sound) throughout a cloud. If the cloud was initially of constant density and in pressure equilibrium with the uniform ambient medium, it will be uniformly heated. Consequently, the cloud will expand without changing its shape and without gaining net momentum (i.e., it will behave like an expanding balloon for weak irradiation or an exploding sphere for strong irradiation). We will refer to such cases as simple example I.

Another class of trivial solutions exists for optically thin clouds with pure scattering opacity. Then again the radiation would propagate throughout the cloud very fast and afterward the cloud would experience a uniform acceleration away from the radiation source. The acceleration would be constant also with time (for small clouds far from the radiation source) and the cloud would gain momentum without changing its size and shape and without mass loss (i.e., in some respects, it will behave like a bullet). We will refer to such cases as simple example II.

Another simple yet non-trivial example, is when a cloud is very optically thick due to absorption opacity and it is exposed to weak radiation. In such a case, the part of the cloud facing the radiation source will be gently heated and the radiation will penetrate only a thin layer of the cloud. The IF and TF would move very slowly across the cloud and there would be no shock. In addition, the cloud would slowly lose mass from its heated part and would be in a quasi-steady state. This simple case and the early evolution of other special cases can be and have been studied using analytic methods that have made various simplifying assumptions in order to estimate for example, the mass loss rate, the final velocity of the neutral cloud, and shape of the IF (e.g., Oort & Spitzer 1955; Bertoldi 1989).

### 1.2. Clouds in AGN

It is challenging to determine what type of clouds are most relevant in a given environment. It is especially true for the so-called Broad Line Regions (BLRs) in AGN because they are spatially unresolved. In most studies that aim at interpreting or modeling the observed line emission and absorption produced in the BLRs, the cloud propriety – such as the density, size, and shape – have been assumed (e.g., Mathews 1974; Blumenthal & Mathews 1975, 1979; Capriotti et al. 1981; Mathews 1982; Arav & Li 1994; Krolik 1999, and references therein).

The presence of broad emission lines (BELs) and broad absorption lines (BALs) in AGN spectra shows that AGN continuum radiation affects the AGN’s immediate environment. BELs are one of the defining spectral features of AGN. They are observed in optical and ultraviolet (UV) spectra and have line wings extending to velocities up to  $10^4$  km s<sup>-1</sup>. It is well established that the primary physical mechanism for production of BELs is photoionization by the compact continuum source of AGN (e.g. Kwan & Krolik 1981; Ferland & Elitzur 1984; Ferland et al. 1998; Hamann & Ferland 1999; Krolik 1999, and references therein). Detailed photoionization calculations presented in these and other studies yield

relatively tight constraints on some physical conditions of the emitting gas (e.g., the gas temperature,  $T_g \approx 10^4$  K, the number density,  $n \approx 10^9$  cm<sup>-3</sup>, the column density  $N \gtrsim 10^{22}$  cm<sup>-2</sup>, and the ionizing flux,  $F_{ion}$  is so high that the ratio between the radiation to gas pressure  $\Xi \equiv F_{ion}/cnkT \approx 1$ ).

The width of BELs indicates that the emitting gas is highly *supersonic*. The shape and position of the BEL profiles has been traditionally explained by lines emitted in a cloudy region without a preferred velocity direction and with a nearly spherical distribution (e.g., Urry & Padovani 1995; Krolik 1999, and references therein). We note that another possibility is that the BEL are produced at the base of a wind from an accretion disk (e.g., Murray et al. 1995; Bottorff et al. 1997).

The key issues that any cloudy model for the BLRs faces are stability and confinement of the clouds (see Osterbrock & Mathews 1986; Krolik 1999; Krause et al. 2012, for reviews). In short, the clouds in the BLRs are hydrodynamically unstable, the nature of their confinement is unclear, while the production of new clouds appears to be inefficient and requires rather extreme conditions. In addition, it has been argued that radiation would cause significant shearing and destroy the clouds before they could contribute to the line emission (e.g., Krolik 1988; Mathews & Doane 1990).

As we mentioned earlier, modeling irradiated clouds is a very challenging problem. Many previous studies of clouds in AGN used various simplifying assumptions and the robustness and applicability of their results remain quite uncertain. Perhaps the most robust results of the previous work is that BELs in AGN are produced by a photoionized and supersonic medium that is optically thick (i.e.,  $N > 10^{22}$  cm<sup>-2</sup>) (e.g., Kwan & Krolik 1981; Ferland & Elitzur 1984; Snedden & Gaskell 2007; Rees et al. 1989). If this medium is indeed made of optically thick clouds then one must accurately treat RT, in particular, shadows. This requires solving self-consistently time-dependent, multidimensional RHD equations.

The direction of the flux is not known independently of the energy density. Therefore, methods based on the diffusion approximation cannot represent shadows. This has been demonstrated through the irradiation of very optically thick structures with a beamed radiation field (e.g., Hayes & Norman 2003; González et al. 2007). However, there are other methods, like the variable Eddington tensor (VET) method that can capture shadows accurately.

For example, Davis et al. (2012) have developed algorithms to solve the RT equation using short characteristics to compute the VET. The tests described in Davis et al. (2012) show the accuracy of the RT solver for two radiation beams (see Figure 6 of that paper). This solver was implemented in the R-MHD code Athena (Stone et al. 2008; Jiang et al. 2012). Jiang et al. (2012) presented some results from a few test runs of the dynamical evolution of a cloud ablated by an intense radiation field. These tests show that the HD as well as MHD solvers implemented in Athena when coupled with the VET method capture shadows correctly. In particular, by using an input radiation field at two angles, Davis et al. (2012) and Jiang et al. (2012) explored

tests where both umbra and penumbra are formed. This makes the tests more difficult, because ad-hoc closures that capture only one direction for the flux will not represent both the umbra and penumbra correctly.

Here, using Athena we study the time evolution of clouds irradiated by a radiation field as strong as the field believed to irradiate the gas in AGN (i.e., radiation pressure to be comparable to gas pressure). We consider clouds with a range of properties: from optically thin to thick and with the opacity due to scattering or absorption processes or both. To explain BELs and BALs, clouds in AGN must move with large velocities. Therefore, our primary focus is on identifying physical conditions under which a pre-existing cloud could be significantly accelerated before it is dispersed.

Athena allows us to explore the above mentioned wide range of conditions. Nevertheless, our treatment of clouds is quite simplified. For example, our simulations are in two-dimensions (2-D) and we assume the clouds to be highly ionized. Therefore, we do not follow the development and evolution of the IF. Moreover, we do not include dust grains and magnetic fields. These and other complications could be modeled with the code but are beyond the scope of this preliminary work.

The outline of this paper is as follows. We describe our calculations in § 2. In § 3, we present our results. We summarize our results and discuss them together with their limitations in § 4.

## 2. METHODS

We solve the radiation hydrodynamic equations in the mixed frame with radiation source terms given by Lowrie et al. (1999). We assume local thermal equilibrium (LTE) and that the Planck and energy mean absorption opacities are the same. Detailed discussion of the equations we solve can be found in Jiang et al. (2012). The equations are

$$\begin{aligned} \frac{\partial \rho}{\partial t} + \nabla \cdot (\rho \mathbf{v}) &= 0, \\ \frac{\partial(\rho \mathbf{v})}{\partial t} + \nabla \cdot (\rho \mathbf{v} \mathbf{v} + \mathbf{P}) &= -\tilde{\mathbf{S}}_{\mathbf{r}}(\mathbf{P}), \\ \frac{\partial E}{\partial t} + \nabla \cdot [(E + P)\mathbf{v}] &= -c\tilde{S}_r(E), \\ \frac{\partial E_r}{\partial t} + \nabla \cdot \mathbf{F}_r &= c\tilde{S}_r(E), \\ \frac{1}{c^2} \frac{\partial \mathbf{F}_r}{\partial t} + \nabla \cdot \mathbf{P}_r &= \tilde{\mathbf{S}}_{\mathbf{r}}(\mathbf{P}). \end{aligned} \quad (1)$$

Here,  $\rho$  is density,  $\mathbf{P} \equiv P\mathbf{l}$  with  $\mathbf{l}$  the unit tensor and  $P$  gas pressure, and  $c$  is the speed of light. The total gas energy density is

$$E = E_g + \frac{1}{2}\rho v^2, \quad (2)$$

where  $E_g$  is the internal gas energy density. We adopt an equation of state for an ideal gas with adiabatic index  $\gamma$ , thus  $E_g = P/(\gamma - 1)$  and  $T = P/R_{\text{ideal}}\rho$ , where  $R_{\text{ideal}}$  is the ideal gas constant. The radiation pressure  $\mathbf{P}_r$  is related to the radiation energy density  $E_r$  by the closure relation

$$\mathbf{P}_r = f E_r. \quad (3)$$

where  $f$  is the VET, and  $\mathbf{F}_r$  is radiation flux. Finally,  $\tilde{\mathbf{S}}_{\mathbf{r}}(\mathbf{P})$  and  $\tilde{S}_r(E)$  are the radiation momentum and energy source terms, respectively.

Following Jiang et al. (2012), we use a dimensionless set of equations and variables in the remainder of this work. We convert the above set of equations to the dimensionless form by choosing fiducial units for temperature, pressure, and velocity as  $T_0$ ,  $P_0$ , and  $a_0 = \sqrt{P_0/T_0}$ , respectively. Then units for radiation energy density  $E_r$  and flux  $\mathbf{F}_r$  are  $a_r T_0^4$  and  $c a_r T_0^4$ . In other words,  $a_r = 1$  in our units. The dimensionless speed of light is  $\mathbb{C} \equiv c/a_0$ . The original dimensional equations can then be written in the following dimensionless form

$$\begin{aligned} \frac{\partial \rho}{\partial t} + \nabla \cdot (\rho \mathbf{v}) &= 0, \\ \frac{\partial(\rho \mathbf{v})}{\partial t} + \nabla \cdot (\rho \mathbf{v} \mathbf{v} + \mathbf{P}) &= -\mathbb{P} \mathbf{S}_{\mathbf{r}}(\mathbf{P}), \\ \frac{\partial E}{\partial t} + \nabla \cdot [(E + P)\mathbf{v}] &= -\mathbb{C} S_r(E), \\ \frac{\partial E_r}{\partial t} + \mathbb{C} \nabla \cdot \mathbf{F}_r &= \mathbb{C} S_r(E), \\ \frac{\partial \mathbf{F}_r}{\partial t} + \mathbb{C} \nabla \cdot \mathbf{P}_r &= \mathbb{C} \mathbf{S}_{\mathbf{r}}(\mathbf{P}), \end{aligned} \quad (4)$$

where the dimensionless source terms are,

$$\begin{aligned} \mathbf{S}_{\mathbf{r}}(\mathbf{P}) &= -\sigma_t \left( \mathbf{F}_r - \frac{\mathbf{v} E_r + \mathbf{v} \cdot \mathbf{P}_r}{\mathbb{C}} \right) + \sigma_a \frac{\mathbf{v}}{\mathbb{C}} (T^4 - E_r), \\ S_r(E) &= \sigma_a (T^4 - E_r) + (\sigma_a - \sigma_s) \frac{\mathbf{v}}{\mathbb{C}} \cdot \left( \mathbf{F}_r - \frac{\mathbf{v} E_r + \mathbf{v} \cdot \mathbf{P}_r}{\mathbb{C}} \right), \end{aligned} \quad (5)$$

while  $\sigma_a$  and  $\sigma_s$  are the absorption and scattering opacities. Total opacity (attenuation coefficient) is  $\sigma_t = \sigma_s + \sigma_a$ . The dimensionless number  $\mathbb{P} \equiv a_r T_0^4 / P_0$  is a measure of the ratio between radiation pressure and gas pressure in the fiducial units. We prefer the dimensionless equations because the dimensionless numbers, such as  $\mathbb{C}$  and  $\mathbb{P}$ , can quantitatively indicate the importance of the radiation field as discussed in Jiang et al. (2012).

We solve these equations in a 2D  $x - y$  plane with the recently developed radiation transfer module in Athena (Jiang et al. 2012). The continuity equation, gas momentum equation and gas energy equation are solved with a modified Godunov method, which couples the stiff radiation source terms to the calculations of the Riemann fluxes. The radiation subsystem for  $E_r$  and  $\mathbf{F}_r$  are solved with a first order implicit Backward Euler method. Details on the numerical algorithm and tests of the code are described in Jiang et al. (2012). The variable Eddington tensor is computed from angular quadratures of the specific intensity  $I_r$ , which is calculated from the time-independent transfer equation

$$\frac{\partial I_r}{\partial s} = \kappa_t (S - I_r). \quad (6)$$

Details on how we calculate the VET, including tests, are given in Davis et al. (2012).

Most of our simulations are performed using our standard computational domain  $(x_{\min}, x_{\max}) \times (y_{\min}, y_{\max})$  which is  $(-0.5, 0.5) \times (-0.5, 0.5)$  and standard resolution which is  $512 \times 512$  cells. Initially the background medium has density  $\rho_0 = 1 \text{ g/cm}^3$  and tem-

perature  $T_0 = 10^6$  K. An over-dense clump is located in a circular region  $r \equiv x^2/x_0^2 + y^2/y_0^2 \leq 1$ , with  $x_0 = y_0 = 0.05$  cm. The density inside this region is  $\rho(x, y) = \rho_0 + (\rho_1 - \rho_0)/[1.0 + \exp(10(r - 1))]$ , where  $\rho_1$  is a free parameter. The clump is in pressure equilibrium with its surroundings, so the interior is colder than the ambient medium. The initial radiation temperature is the same as the gas temperature everywhere. Here we consider opacities due to scattering,  $\sigma_s = \sigma_{s,0}(\rho/\rho_0)$ , or absorption  $\sigma_a = \sigma_{a,0}(T/T_0)^{-3.5}(\rho/\rho_0)^2 \text{ cm}^{-1}$ , or both  $\sigma_t = \sigma_s + \sigma_a$ . The radiation flux  $\mathbf{F}_r$  is zero everywhere initially. We use reflection boundary conditions on both  $y$  boundaries, outflow boundary conditions on the right  $x$  boundary. A constant radiation field with temperature  $T_r = 2T_0$  is input through the left  $x$  boundary. At the left  $x$  boundary, the gas temperature and density are fixed to  $T_0$  and  $\rho_0$  respectively. The dimensionless speed of light  $\mathbb{C} = 3.3 \times 10^3$ , and the parameter  $\mathbb{P} = 10^{-3}$ .

### 3. RESULTS

We have performed over thirty different simulations exploring the parameter space and numerical effects. Here we discuss in some detail five simulations that illustrate the evolution of a cloud in significantly different physical regimes: a optically thin and thick cloud with the pure scattering opacity (runs S10 and S200, respectively) and mildly optically thick, optically thick, and very optically thick cloud with absorption dominated opacity (runs A10, A40, and A80, respectively). Our convention of naming the simulations is the following: the letter A or S stands for the opacity type, i.e., dominated by absorption or scattering, respectively. A number that follows the letter corresponds to the initial cloud density,  $\rho_1$ .

We summarize the properties of the five simulations in Table 1. Columns (2), (3) and (4) give the input physical parameters:  $\sigma_{a,0}$ ,  $\sigma_{s,0}$ , and  $\rho_1$ . In columns (5), (6), (7), (8), and (9) we list the following initial properties of the cloud: the absorption optical depth,  $\tau_a = 2x_o\sigma_a$ , the scattering optical depth,  $\tau_s = 2x_o\sigma_s$ , the radiation diffusion time across the cloud,  $t_{dif} = 4x_o^2\sigma_t/\mathbb{C} = \tau_t t_{fs}$ , where  $t_{fs} = 2x_o/\mathbb{C}$  is the free-streaming time<sup>5</sup>, the thermal time scale inside the cloud,  $t_{th} = P/(\mathbb{P}C E_r \sigma_a)$ , and the sound crossing time  $t_{sc} = 2x_o/c_s$ , where  $c_s = \sqrt{\gamma P/\rho}$  is the adiabatic sound speed. Finally, columns (10), (11), and (12) give the numerical resolution,  $n_x \times n_y$ , the Courant number,  $C_0$ , and the final time at which we stopped each simulation,  $t_f$ . For the five runs, we used our standard computational domain.

Figure 1 gives an overview of the cloud evolution in the five runs (columns from left to right correspond to runs: S10, S200, A10, A40, and A80). Specifically, the figure shows sequences of density maps overlaid with velocities at five different times (the time increases from top to bottom; the actual time is given in the top left corner in each panel).

Figure 2 shows several cloud properties as a function of time. The figure illustrates more qualitatively the differences between various runs (the columns' correspondence to various runs is the same as in Fig. 1) as well as dramatic changes in the clouds with time.

To illustrate how a given cloud would appear to an observer measuring the radiation at the right side of the

computational domain, the panels in the top row present the  $x$  component of the normalized radiation field,  $F_{r,1}$ , as a function of the  $y$  coordinate. The second from top row of panels show  $F_{r,1}$  at the right boundary but only at  $y = 0$  (i.e. the  $(x_{max}, 0)$  location) and its minimum value along the right boundary (the dashed and solid lines, respectively). The fluxes in these panels are normalized so that they are in units of the maximum radiation flux along the right boundary at a given time. The middle panels present the time evolution of the *cold* gas in the computational domain: the maximum density, total mass and the mass loss rate of the cold gas (the solid, dotted, and dashed lines, respectively). We normalized the maximum density to the initial density of the cloud,  $\rho_1$ . Our operational definition of ‘‘cold’’ gas is the gas with the temperature less than 2 times the initial temperature of the cloud. Therefore, the middle row panels can be used to follow the cloud heating and subsequent evaporation.

To follow the average cloud motion, the second bottom row of panels show the  $x$ -position of the center of mass (CoM) of the cold gas, while the bottom panels show the  $x$  component of the CoM velocity and the maximum velocity of the cold gas (the solid and dash-dotted lines, respectively).

We start by discussing run S10 that is related to one of the simple cases mentioned in § 1.1: simple example II, with scattering opacity only and relatively small optical depth (i.e.,  $\tau_s = 0.2$ ). The left columns of panels of Figs. 1 and 2 show that, as expected, there is no compression (i.e.,  $\rho_{max} = 1$ ) no loss of the cold gas, and no shock formation. The cloud is almost uniformly accelerated in the horizontal direction. The implied mass loss of cold gas for  $t \geq 27$  is simply the result of the cold cloud being advected out of the domain. In addition, the cloud is almost co-moving with the ambient medium. We note that the acceleration due to the radiation force,  $a_{rad}$  is almost position and time independent in this optically thin case, i.e.,  $a_{rad} = \mathbb{P}\sigma_{s,0}F_{r,1} \simeq 1.6 \times 10^{-3}$  (one can ignore the velocity dependent terms in the source term,  $\mathbf{S}_r(\mathbf{P})$ , in the momentum equation as these terms are very small, i.e.,  $v/\mathbb{C} \ll 1$ ). This acceleration is relatively small. Specifically, the time for an optically thin fluid element to travel a distance equal to the cloud diameter,  $t_{dyn} = (4x_o/a_{rad})^{1/2} \approx 11$  is long compared to  $t_{sc} = 0.24$ .

Also as expected, the position of CoM is a quadratic function of time and the maximum velocity of the cold gas is very similar to the velocity of CoM (see the two lowest panels of the left hand side column in Fig. 2). The small but not zero optical depth means that the front side of the cloud experiences a slightly stronger push by radiation than the back side (the acceleration at the back compared to that at the front is smaller by a factor of 0.9). Consequently, the cloud is flattened by radiation. This effect is much stronger in run S200, where the cloud is optically thick.

The second left column of panels in Figure 1 illustrate how the radiation initially ‘squeezes’ the cloud in S200: the front side is pushed by radiation while the back side does not move. The radiation pressure acts only from the left side and the gas pressure inside the cloud is higher than the pressure of the ambient gas. This pressure imbalance leads to lateral expansion that is notice-

<sup>5</sup>  $t_{fs} = 6.06 \times 10^{-5}$  and it is the same for all the cases discussed.

able already by the time,  $t = 12$ . The cloud evolution is further complicated by the fact that the optical depth decreases (not always monotonically) as a function of  $y$  from the cloud center to its edge. For example, as the cloud moves as a whole to the right it also expands laterally and its shape starts to resemble a crescent because the more transparent edges are pushed more than the cloud center.

The top panel in the second left column in Figure 2 shows clearly that the shadow size increases with time. However, the panel also shows that at the later times (i.e.,  $t \gtrsim 20$ ) the cloud center is not the most opaque part of the cloud. Instead the most opaque regions are near the edges where the horns of the crescent bend over toward the center (the second top panel shows this too: for  $t \gtrsim 20$ , the minimum radiation field along the  $y$  direction at  $x = x_{max}$  is not at  $y = 0$ ).

Overall the cloud in run S200 moves slower than in run S10 (compare the second to bottom and bottom panels in corresponding columns in Fig. 2). In addition, for run S200, the CoM velocity is lower than the maximum velocity of the cold gas. This difference in the velocities is an indication of a non-uniform cloud evolution. The two just presented examples show that even for a pure scattering opacity case, the cloud evolution is fast and very different than the movement of a bullet where there is no change in the shape and size as the cloud moves. The evolution of a cloud with absorption dominated opacity is even more dynamic and complex and also faster.

We start by discussing run A10 that is related to another simple case mentioned in § 1.1: simple example I - the cloud behaving as a balloon. In this run,  $\tau_a = 2 \times 10^3$ ,  $t_{dif} = 1.2 \times 10^{-1}$ , while  $t_{th} = 2 \times 10^{-6}$ . Thus, both  $t_{dif}$  and  $t_{th}$  are much smaller than  $t_{dyn}$ . Therefore, the evolution of the absorption dominated cases is much faster than the pure scattering cases. For example, the middle column of panels of Fig. 1 show that the cloud expands within time less than 0.2. During its evolution, the cloud does not gain much net momentum and it remains almost spherical.

The total mass of the cold gas drops to zero within  $t = 3 \times 10^{-2}$  (see the middle panel in the middle column in Fig. 2). This time is of the order of  $t_{dif}$ . The gas density in the cloud is initially increased by a factor of 2 but for  $t \gtrsim 0.05$   $\rho_{max}$  decreases below 0.01. We note that in this run, the velocity of CoM does not correspond to the movement of the whole cloud but rather to the change in the location of the boundary between the cold and hot (to the rapid propagation of TF). Hence, the implied CoM velocity can exceed the maximal velocity in these runs. The bottom panel in the middle column of Figure 2 shows that for as long as the cold gas exists, its velocity increases very fast with time. After  $t_{dif}$ , the only gas left on the grid is the transparent and hot gas moving almost radially away from the center of the grid where the initial cloud was located.

The cloud in run A10 is initially optically thick. However, once the fast TF passes the cloud, the optical depth drops to about 0.6 due to an increase of the temperature alone (i.e., with small change in the cloud density). This quick, isochoric decrease in the cloud optical depth is the main reason for the evolution in run A10 to resemble the evolution of simple example I which we referred to as an expanding balloon. Runs with  $\tau_a$  lower than in run A10

show very similar evolution but occurring on a longer time scale. However runs with higher optical depth show substantial qualitative differences. A good indicator of the expected difference in the evolution is the relation between the diffusion and sound crossing times.

For run A10,  $t_{dif} < t_{sc}$  and the cloud behaves like a balloon even though it is initially optically thick. However, for run A40 with  $t_{dif} > t_{sc}$  (and  $t_{th}$  shortened by almost 4 orders of magnitude), we observe strong evaporation from the irradiated side, the development and propagation of a strong shock inside the cloud, and a few other features unseen in run A10 (compare the middle and second right columns of panels in Figs. 1 and 2).

In run A40, the radiation heats the front much faster than it can diffuse across the cloud. Therefore, the cloud loses mass from the left side through a hot outflow. In addition, a very fast and strong shock propagates to the right of the cloud compressing it and changing its shape. The changes in the shape are major: from the initial convex shape through the concave one of the front side to the break up of the cloud into two smaller elongated clumps.

The cloud evolution is far from being isochoric. For example, the density on the left side of the cold part of the cloud is increased by a factor of 8 (i.e.,  $\rho_{max} = 8$ ) at  $t = 0.9$ . This time corresponds to the maximum compression of the cloud and the smallest shadow (see the fourth column of panels in Figs. 1 and 2). After this time the cloud re-expands and fragments (around  $t = 0.17$ ). Finally, at  $t \approx 0.25$ , even the dense clumps become optically thin as they are heated and dispersed.

As expected, the cloud in run A40 survives much longer than in run A10. Another consequence of the higher cloud density is that the dense parts of the cloud can travel over some distance before they are heated and dispersed. For example, the second bottom panel in the fourth column of Fig. 1 shows two dense and optically thick clumps at  $x = 0.18$  for  $t=0.20$  - more than three radii of the initial cloud away from the original location. This cloud movement to the right is caused by the cloud hot outflow that moves to the left (i.e., the rocket effect). The push by radiation pressure in this run as well as in runs A10 and A80 is negligible because  $t_{dyn} \approx 11$  which is orders of magnitude longer than  $t_{th}$ .

To show the evolution of an even denser cloud, we carried out a simulation for  $\rho_1 = 80$  (run A80). The right hand side panels of Figs. 1 and 2 show the results of this simulation. Overall, the evolution of this denser cloud resembles that of the cloud in run A40. However, there are some quantitative differences. In particular, in run A80, the cloud stays optically thick for about twice as long as in run A40 (compare the second top panels in the second right and right columns in Fig. 2). The two clumps that form after the re-expansion phase are denser and more elongated.

The middle to bottom panels in the right column of the figure suggest that the cloud disappears at  $t \approx 0.13$  and reappears around 0.24. However, this is an artifact of our formal definition of the cold phase (the gas with the temperature less than 2 times the initial temperature of the cloud). The 'disappearance' of the cold phase corresponds the smallest cloud size with the gas temperature increased due to compression rather than radiative heating. However, as the dense cloud later re-expands, the

gas temperature drops below our temperature threshold. Later still, the cloud moves to the right, fragments and continues to be heated by radiation so that at  $t \approx 0.40$  it is totally dispersed.

#### 4. SUMMARY AND DISCUSSION

We have presented two-dimensional, radiation-hydrodynamic calculations of time-dependent structure of strongly irradiated clouds. Our primary conclusions are the following: 1) even a relatively dense cloud that is radiatively heated (i.e., with significant absorption opacity) does not move as a whole, and instead undergoes a very dramatic evolution in its shape, size and physical properties. In particular, the cloud and its remnants become optically thin within less than one sound crossing time and before they can travel over a significant distance (a distance of a few radii of the initial cloud) and 2) a cloud can be accelerated as a whole under quite extreme conditions, e.g., the opacity must be dominated by scattering. However, the radiation force acceleration is relatively small and unless the cloud is optically thin, the cloud quickly changes its size and shape.

A competition of several physical processes determines the cloud evolution. In the cases that we have explored, the most important processes are the radiation diffusion and heating, the radiation force acceleration, and finally propagation of the sound speed. Comparing the time scales corresponding to each of these processes (see § 1), one can predict the behaviour of a cloud with given initial conditions. For example, as we noted in § 3, for absorption dominated opacity and  $t_{dif} < t_{sc}$ , a cloud will behave like a balloon (simple example I) even if the cloud is initially optically thick. The radiative heating is usually the fastest process. Therefore, simple example II (a bullet like case) requires very special conditions: scattering dominated opacity and the optical depth much less than one.

Our goal here was to carry out simulations in a simple and well-controlled way so that we can assess the role of the type and magnitude of the opacity on the cloud evolution. While achieving this goal, we found that Athena can handle well quite a wide range of physical conditions. Not surprisingly, we also found that the most difficult cases to compute are those with huge density and opacity contrasts, especially when the opacity is dominated by absorption. In these cases, the thermal time scale can be extremely short so that the equation of energy is stiff. To avoid spurious oscillations, we had to increase the numerical resolution and reduce the Courant number (see columns 10 and 11 in Table 1). For example, in run A80, we reduced  $C_0$  to 0.02 from its usual value of 0.8.

In the runs discussed here, we increased the temperature of the incoming radiation by a relatively small factor of 2 ( $T_r = 2T_0$ ). This corresponds to an increase of the radiation pressure by a factor of 16. Results from our various tests with higher  $T_r$  and also higher  $\mathbb{P}$  confirm simple expectations that increasing  $T_r$  or  $\mathbb{P}$  results in a faster cloud evolution because of the increases in the heating rate and cloud acceleration.

As we mentioned in § 1, the clouds in the BLRs are optically thick to absorption and optically thin to scattering. Therefore, the results from runs A40 and A80 are most applicable to the BLRs of AGN. These results well

illustrate the fact that any cloudy model for the BLRs faces the issues of stability and confinement.

These are very serious issues because in our simplified simulations, the cloud velocity was not very different from the ambient velocity. In particular, we did not assume that the cloud is on a Keplerian orbit around the central black hole as it is assumed in some BLR models (e.g., Pancoast et al. 2011; Krause et al. 2012, and references therein). Therefore, here the cloud was not much affected by hydrodynamic instabilities caused by velocity shear. Nevertheless, we found that the cloud can not be significantly accelerated before it is dispersed (i.e., the rocket effect is not efficient). The main process responsible for the dispersal is radiative heating. One of the implications of these results is that clouds in the BLRs, if they exist, likely take on many different and complex shapes and this complication should be considered in detailed calculations of cloud line emission.

There are a number of limitations to our results. Probably the most important are that we neglected gas photoionization and assumed frequency-independent (gray) opacities. Additional limitations to our calculations are that they are 2-D instead of fully 3-D and that we did not include thermal conduction, magnetic fields, and the process or processes responsible for the cloud formation. Moreover, in realistic simulations of the BLRs, one should also consider computing the evolution of interacting multiple clouds with various properties, not just one cloud as we did here. Our results indicate that such multi-cloud simulations are feasible using Athena.

We plan to go beyond some of these limitations in the near future. In particular, we plan to address the issue of cloud formation and subsequent evolution. One possible approach would be to consider the radiative processes and conditions for which the gas is thermally unstable so that cold condensations can grow on relatively short time scales despite the presence of a strong radiation field (e.g., Krolik 1988; Mościbrodzka & Proga 2013, and references therein). Such an approach, our intended next step, will involve simulations quite different from those presented here because among other things, here the gas is thermally stable and initially it is not in a radiative equilibrium.

#### ACKNOWLEDGMENTS

This work was supported by NASA under ATP grant NNX11AI96G and NNX11AF49G. D.P. thanks S. Lepp for discussions and also the Department of Astrophysical Sciences, Princeton University for its hospitality during his sabbatical when the work presented here was initiated. He also wishes to acknowledge the National Supercomputing Center for Energy and the Environment, for providing computer resources and support. Y.F.J. was provided by NASA through Einstein Postdoctoral Fellowship grant number PF-140109 awarded by the Chandra X-ray Center, which is operated by the Smithsonian Astrophysical Observatory for NASA under contract NAS8-03060.

#### REFERENCES

- Arav, N., & Li, Z.-Y. 1994, ApJ, 427, 700
- Bally, J. 1995, in Lecture Notes in Physics, Berlin Springer Verlag, Vol. 459, The Physics and Chemistry of Interstellar Molecular Clouds, ed. G. Winnewisser & G. C. Pelz, 118–119

- Bertoldi, F. 1989, *ApJ*, 346, 735
- Bertoldi, F., & McKee, C. F. 1990, *ApJ*, 354, 529
- Blumenthal, G. R., & Mathews, W. G. 1975, *ApJ*, 198, 517
- Blumenthal, G. R., & Mathews, W. G. 1979, *ApJ*, 233, 479
- Bottorff, M., Korista, K. T., Shlosman, I., & Blandford, R. D. 1997, *ApJ*, 479, 200
- Capriotti, E., Foltz, C., & Byard, P. 1981, *ApJ*, 245, 396
- Castor, J. I. 2004, *Radiation Hydrodynamics*, by John I. Castor, pp. 368. ISBN 0521833094. Cambridge, UK: Cambridge University Press, November 2004.,
- Davis, S. W., Stone, J. M., & Jiang, Y.-F. 2012, *ApJS*, 199, 9
- Donahue, M., & Shull, J. M. 1987, *ApJ*, 323, L13
- Ferland, G. J., & Elitzur, M. 1984, *ApJ*, 285, L11
- Ferland, G. J., Korista, K. T., Verner, D. A., et al. 1998, *PASP*, 110, 761
- González, M., Audit, E., & Huynh, P. 2007, *A&A*, 464, 429
- Hamann, F., & Ferland, G. 1999, *ARA&A*, 37, 487
- Hayes, J. C., & Norman, M. L. 2003, *ApJS*, 147, 197
- Jiang, Y.-F., Stone, J. M., & Davis, S. W. 2012, *ApJS*, 199, 14
- Krause, M., Burkert, A., & Schartmann, M. 2011, *MNRAS*, 411, 550
- Krause, M., Schartmann, M., & Burkert, A. 2012, *MNRAS*, 425, 3172
- Krolik, J. H. 1999, *Active galactic nuclei : from the central black hole to the galactic environment* /Julian H. Krolik. Princeton, N. J. : Princeton University Press, c1999.,
- Krolik, J. H. 1988, *ApJ*, 325, 148
- . 2007, *ApJ*, 661, 52
- Kwan, J., & Krolik, J. H. 1981, *ApJ*, 250, 478
- Lefloch, B., & Lazareff, B. 1994, *A&A*, 289, 559
- Lowrie, R. B., Morel, J. E., & Hittinger, J. A. 1999, *ApJ*, 521, 432
- Mathews, W. G. 1974, *ApJ*, 189, 23
- Mathews, W. G. 1982, *ApJ*, 252, 39
- Mathews, W. G. 1983, *ApJ*, 272, 390
- Mathews, W. G. 1986, *ApJ*, 305, 187
- Mathews, W. G., & Blumenthal, G. R. 1977, *ApJ*, 214, 10
- Mathews, W. G., & Capriotti, E. R. 1985, *Astrophysics of Active Galaxies and Quasi-Stellar Objects*, 185
- Mathews, W. G., & Doane, J. S. 1990, *ApJ*, 352, 423
- McKee, C. F., & Ostriker, E. C. 2007, *ARA&A*, 45, 565
- Mellema, G., Raga, A. C., Canto, J., et al. 1998, *A&A*, 331, 335
- Mihalas, D., & Mihalas, B. W. 1984, *Foundations of radiation hydrodynamics*, ed. Mihalas, D. & Mihalas, B. W.
- Mościbrodzka, M., & Proga, D. 2013, *ApJ*, 767, 156
- Murray, N., Chiang, J., Grossman, S. A., & Voit, G. M. 1995, *ApJ*, 451, 498
- Oort, J. H., & Spitzer, L., Jr. 1955, *ApJ*, 121, 6
- Osterbrock, D. E. 1974, *Research supported by the Research Corp., Wisconsin Alumni Research Foundation, John Simon Guggenheim Memorial Foundation, Institute for Advanced Studies, and National Science Foundation. San Francisco, W. H. Freeman and Co., 1974. 263 p.,*
- Osterbrock, D. E., & Mathews, W. G. 1986, *ARA&A*, 24, 171
- Pancoast, A., Brewer, B. J., & Treu, T. 2011, *ApJ*, 730, 139
- Raga, A. C., Esquivel, A., Riera, A., & Velázquez, P. F. 2007, *ApJ*, 668, 310
- Rees, M. J., Netzer, H., & Ferland, G. J. 1989, *ApJ*, 347, 640
- Stone, J. M., Gardiner, T. A., Teuben, P., Hawley, J. F., & Simon, J. B. 2008, *ApJS*, 178, 137
- Snedden, S. A., & Gaskell, C. M. 2007, *ApJ*, 669, 126
- Urry, C. M., & Padovani, P. 1995, *PASP*, 107, 803

**Table 1**  
Summary of runs

Run	$\sigma_{a,0}$	$\sigma_{s,0}$	$\rho_1$	$\bar{\tau}_a$	$\bar{\tau}_s$	$t_{dif}$	$t_{th}$	$t_{sc}$	$n_x \times n_y$	$C_o$	$t_f$
S10	0	0.1	10	0	0.2	-	$\infty$	0.48	$512 \times 512$	0.8	50
S200	0	0.1	200	0	4.0	$2.4 \times 10^{-4}$	$\infty$	2.20	$512 \times 512$	0.8	50
A10	$3.16 \times 10^{-2}$	0.1	10	$2 \times 10^3$	0.2	$1.2 \times 10^{-1}$	$2 \times 10^{-6}$	0.48	$1024 \times 1024$	0.1	0.3
A40	$3.16 \times 10^{-2}$	0.1	40	$4 \times 10^6$	0.8	$2.4 \times 10^2$	$9 \times 10^{-10}$	0.98	$1024 \times 1024$	0.1	0.3
A80	$3.16 \times 10^{-2}$	0.1	80	$1.8 \times 10^8$	1.6	$1.2 \times 10^4$	$2 \times 10^{-11}$	1.38	$1024 \times 1024$	0.02	0.6

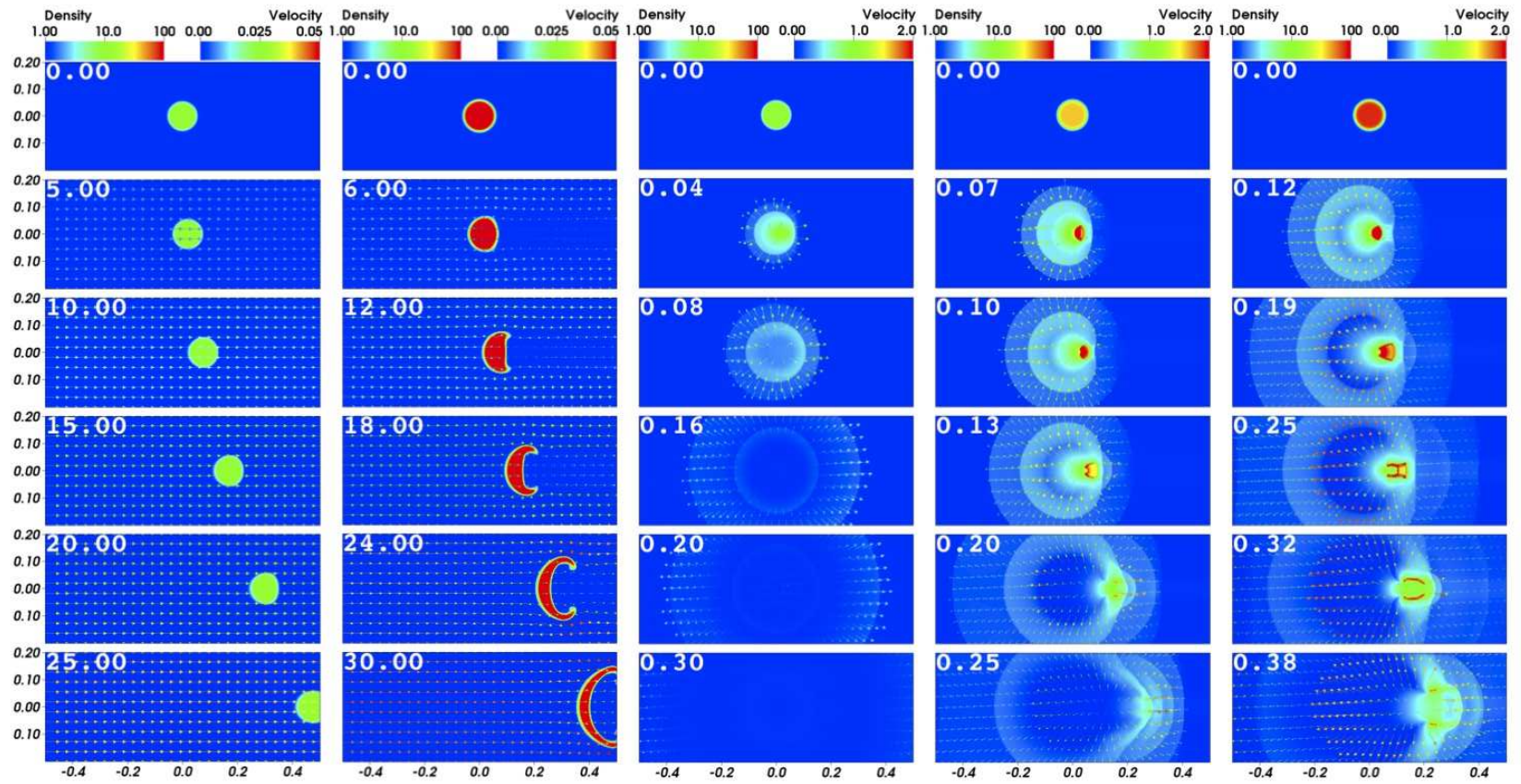


**Figure 1.** Sequences of density maps overlapped by the velocity fields for runs S10, S200, A10, A40 and A80 (from left to right) at five different times shown at the top left corner of each panel (from top to bottom)

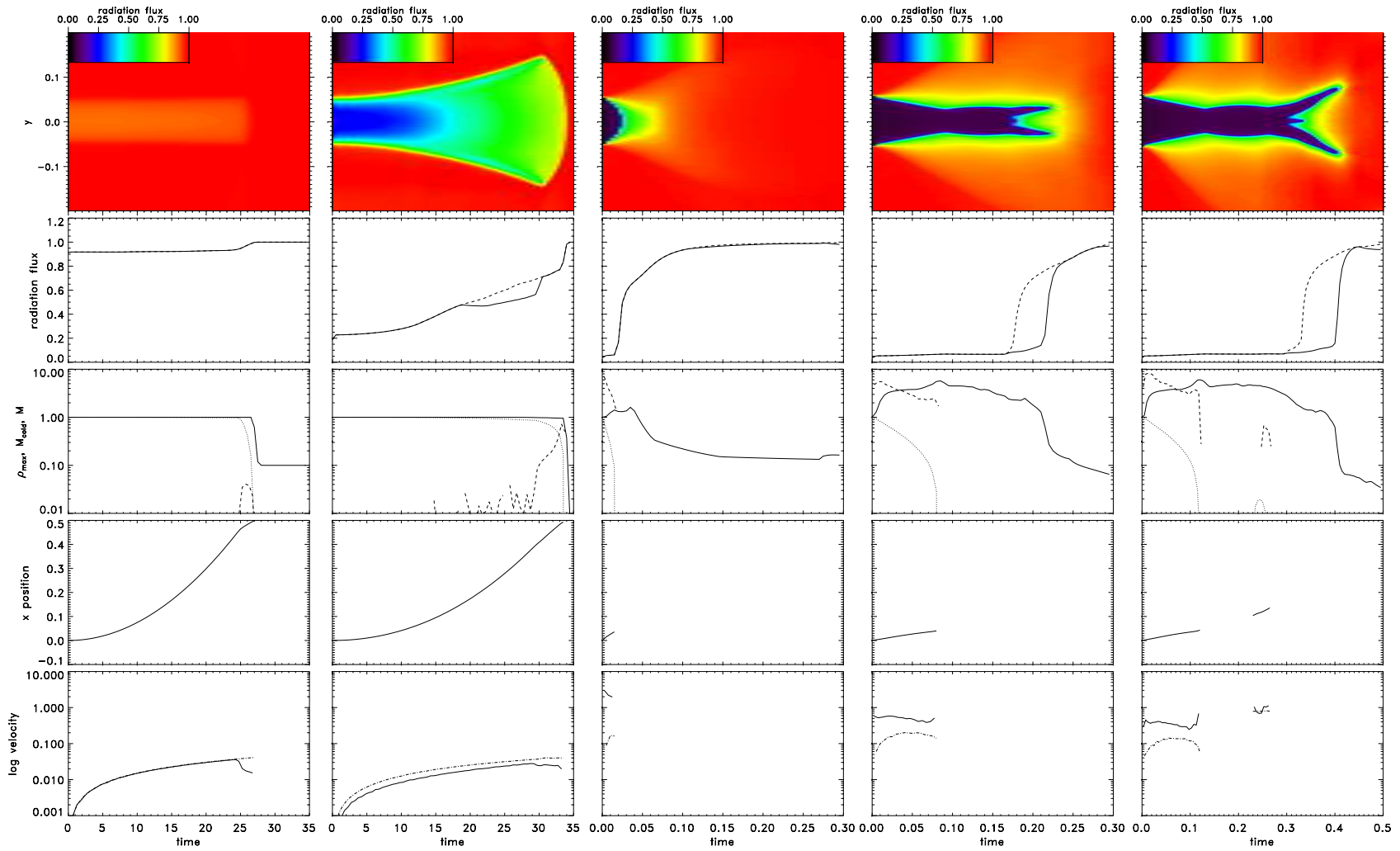


**Figure 2.** Time evolution of various properties for each run (from left to right: run S10, S200, A10, A40, and A80). *From top to bottom:* the  $x$  component of the radiation field,  $F_{r,1}$  as a function of  $y$  along the right boundary of the computational domain (top panels); the minimum value of  $F_{r,1}$  and  $F_{r,1}$  at  $y = 0$  along the right edge of the computational domain, the solid and dashed lines, respectively (second top panels); the total mass and mass loss rate of the cold gas and the maximum density, the dotted, dashed, and solid lines, respectively (middle panels); the  $x$ -position of the center of mass of the cold gas (second bottom panels); the  $x$  velocity of the center of mass and the maximum velocity of the cold gas, the solid and dash-dotted lines (bottom panels). The fluxes in the top and second top panels are normalized so that they are in units of the maximum radiation flux along the right boundary at a given time.